

Development of the microcalorimeter and anticoincidence detector for the Line Emission Mapper x-ray probe

Stephen J. Smith^{a,*} Joseph S. Adams,^{a,b} Simon R. Bandler,^a Rachel B. Borrelli^a,
James A. Chervenak,^a Renata S. Cumbee,^a Enectali Figueroa-Feliciano,^c
Fred M. Finkbeiner^{a,d} Joshua Furhman^{a,b} Samuel V. Hull,^{a,e} Richard L. Kelley,^a
Caroline A. Kilbourne^a Noah A. Kurinsky,^f Jennette N. Mateo^a Asha Rani,^{a,g}
Kazuhiro Sakai^{a,b} Nicholas A. Wakeham^{a,b} Edward J. Wassell,^a and
Sang H. Yoon^{a,g}

^aNASA Goddard Space Flight Center, Greenbelt, Maryland, United States

^bUniversity of Maryland Baltimore County, Center for Space Sciences and Technology, Baltimore, Maryland, United States

^cNorthwestern University, Evanston, Illinois, United States

^dSigma Space Corp./Hexagon US Federal, Lanham, Maryland, United States

^eUniversity of Maryland, Department of Astronomy, College Park, Maryland, United States

^fSLAC National Accelerator Laboratory, Menlo Park, California, United States

^gScience Systems and Applications, Inc. (SSAI), Lanham, Maryland, United States

ABSTRACT. The Line Emission Mapper (LEM) is an x-ray probe mission concept that is designed to provide unprecedented insight into the physics of galaxy formation, including stellar and black-hole feedback and flows of baryonic matter into and out of galaxies. LEM incorporates a light-weight x-ray optic with a large-format microcalorimeter array. The LEM detector utilizes a 14k pixel array of transition-edge sensors (TESs) that will provide <2.5 eV spectral resolution over the energy range 0.2 to 2 keV, along with a field-of-view of 30 arcmin. The microcalorimeter array and readout builds upon the technology developed for the European Space Agency's (ESA's) Athena/x-ray Integral Field Unit. Here, we present a detailed overview of the baseline microcalorimeter design, its performance characteristics, including a detailed energy resolution budget and the expected count-rate capability. In addition, we outline the current status and plan for continued technology maturation. Behind the LEM array sits a high-efficiency TES-based anticoincidence (antico) detector that will reject cosmic-ray background events. We will briefly describe the design of the antico and plan for continued development.

© The Authors. Published by SPIE under a Creative Commons Attribution 4.0 International License. Distribution or reproduction of this work in whole or in part requires full attribution of the original publication, including its DOI. [DOI: [10.1117/1.JATIS.9.4.041005](https://doi.org/10.1117/1.JATIS.9.4.041005)]

Keywords: transition-edge sensor; x-ray detector; imaging spectrometer; superconducting device; x-ray telescope

Paper 23083SS received Jul. 20, 2023; revised Sep. 29, 2023; accepted Oct. 3, 2023; published Oct. 18, 2023.

1 Introduction

The Line Emission Mapper (LEM) is an x-ray probe currently in development (in pre-Phase A) by the Smithsonian Astrophysical Observatory, Goddard Space Flight Center (GSFC), and Lockheed Martin.^{1,2} If selected, it would be launched in the early 2030s. LEM combines a silicon grazing incidence x-ray optic (x-ray mirror assembly) with a cryogenically cooled

*Address all correspondence to Stephen Smith, stephen.j.smith@nasa.gov

microcalorimeter array [LEM microcalorimeter spectrometer (LMS)] to provide unparalleled imaging and spectral resolving capabilities over the soft x-ray energy range (0.2 to 2 keV).

X-ray microcalorimeters are non-dispersive spectrometers that measure the heat resulting from the thermalization of an individual photon in a low heat capacity absorber. Operating at cryogenic temperatures (<100 mK) enables extremely high spectral resolution over a wide band-pass, with resolving powers of ~ 3000 at 6 keV routinely demonstrated. Transition-edge sensors (TESs) are a type of microcalorimeter based on superconducting thin films, voltage biased in the transition region between the onset of resistance and the fully normal state.³ The resistance change is determined by monitoring the current through the TES using a superconducting quantum interference device (SQUID), and a SQUID multiplexing scheme allows for the readout of many pixels.⁴ This technology is well suited to the needs of next generation x-ray satellites, enabling spatially resolved, high throughput observations of extended objects such as galaxy clusters and supernova remnants, with high spectral resolution. The LMS will have a 14k pixel TES array and will be readout using time-division-multiplexing (TDM).⁴ Given the diffuse and faint nature of LEM's targets, a high-fidelity anticoincidence (antico) detector is essential to reduce the instrument background. Situated directly behind the main array, a TES-based antico will flag and reject events due to cosmic rays which could be confused for photons within the LEM science band.

In this paper, we provide an overview of the design and performance characteristics of the LMS and anticoincidence detector. In Sec. 2, we will start by describing the LMS array configuration, performance requirements, and the status of the technology development. We will then discuss the pixel characteristics, energy resolution budget (ERB), and count-rate capability, before describing the plan for continued technology maturation. Finally, in Sec. 3, we will provide a brief description of the antico design, its current status, and the plan for continued development.

2 LMS Microcalorimeter Array

2.1 LMS Performance Requirements and Array Configuration

The performance requirements for the LMS are listed in Table 1 and a schematic layout of the current baseline array is shown in Fig. 1. The baseline LMS microcalorimeter array concept provides a 33' diameter field-of-view (FoV) with 15" pixels (290 μm pixel pitch) and is arranged in hexagonal configuration. A hexagonal layout is preferred to better match to the cylindrical aperture of the magnetic shield design while facilitating easy tiling of composite observations. The large FoV combines with a high effective area (1200 cm^2 at 0.5 keV) to provide LEM with an extremely large grasp (FoV \times area). This enables LEM to efficiently map diffuse, low surface brightness objects with sizes comparable to or greater than the FoV (such as nearby galaxies, clusters, the intergalactic medium, or the Milky Way structures).

The LMS array is a "hybrid" configuration consisting of two different pixel types fabricated on the same substrate. In the current baseline design, the central 7' region of the LMS array consists of 784 independent TES pixels with full width at half maximum (FWHM) spectral

Table 1 Key LMS microcalorimeter performance requirements.

Parameter	Requirement
Energy range	0.2 to 2 keV
FoV	30 arcmin diam.
Angular resolution	18 arcsec
Energy resolution (inner/outer)	1.3/2.5 eV (FWHM) at 1 keV
Energy scale (absolute/relative)	1 eV/0.25 eV at 0.5 keV
Max. background level	2 counts/s/keV/30'

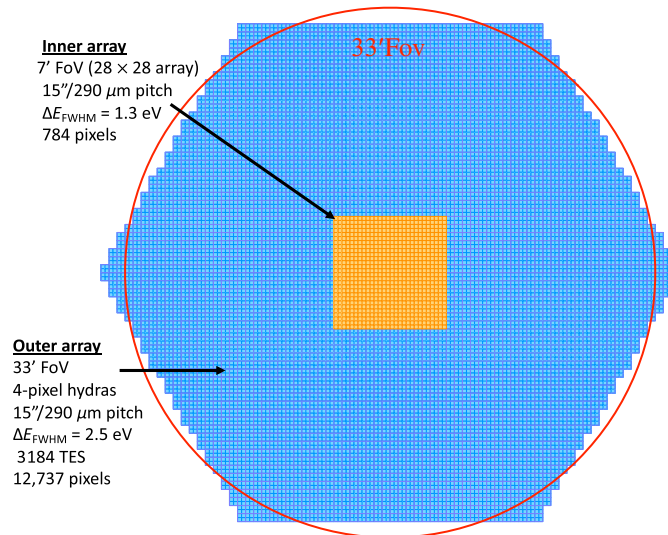


Fig. 1 Schematic layout of LMS sensor array concept consisting of an inner region of $\Delta E_{FWHM} = 1.3$ eV single pixel TESs and an outer region of $\Delta E_{FWHM} = 2.5$ eV 4-pixel hydras. The equivalent diameter of the current baseline array design is 33' (larger than the 30' requirement).

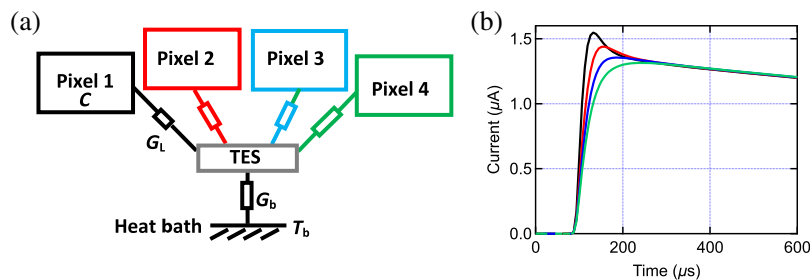


Fig. 2 (a) Simplified thermal model of a 4-pixel hydra. Each absorber is connected to a single TES via a thermal link with different conductance. An x-ray event in each absorber gives rise to a unique pulse shape measured by the TES. (b) Measured average pulse shapes for the four pixels of a LMS hydra showing the initial rising edge of the measured signal, which is used to determine event position. The pulse shape with the fastest rise time corresponds to the pixel with the highest thermal coupling to the TES.

resolution of $\Delta E_{FWHM} = 1.3$ eV at 1 keV. The remainder of the array comprises 3184, 4-pixel hydras with $\Delta E_{FWHM} = 2.5$ eV at 1 keV. Hydras are “thermally multiplexed” TESs consisting of multiple distinct x-ray absorbers, each with a different thermal link to a single TES.^{5–7} The conductance of each link is tuned to produce a unique pulse shape for x-rays absorbed in each of the 4 pixels. The pulse rise-time is used to determine the pixel that absorbed the photon (see Fig. 2). The use of hydras allows for the extremely large number of pixels needed for the LEM array, without a proportional increase in the number of wires, bias circuit, and readout components that would otherwise be necessary. In total, the array will have 13.5k pixels but only 4k TESs. The array will be read out with state-of-the-art TDM, implemented with 59 pixels (and 1 dark pixel for gain tracking) in each of the 69 TDM columns.

2.2 Heritage and Current Technology Readiness Level

The design of LMS instrument takes advantage of decades of development of microcalorimeter detector systems for spaceflight and relies heavily on heritage from the microcalorimeter instrument on Hitomi’s soft x-ray spectrometer (SXS),⁸ and from the twice flown microcalorimeter sounding rocket experiment, Micro-X,⁹ which was the first instance of TES detectors being flown in space. TES microcalorimeters and TDM SQUID readouts are baselined for the X-ray Integral Field Unit (X-IFU) on the Athena x-ray observatory,¹⁰ and TES microcalorimeters are

also baselined for the Lynx x-ray microcalorimeter instrument on the Lynx observatory.^{11,12} Details of the full LMS architecture, including the cooling system, focal plane assembly, and detector chain architecture, can be found in Ref. 13, and here we focus on the development of the detector array.

The Athena/X-IFU detector (being developed by the same team at NASA/GSFC) and more recently the LMS array have been assessed at Technology Readiness Level-5 (TRL) in independent NASA/GSFC technology assessment reviews, with many aspects of their designs consistent with TRL-6. The Athena/X-IFU is currently going through a reformulation exercise but was previously planned as a uniform 2.5k pixel array on a 317 μm pitch. The spectral resolution was 2.5 eV at an energy of 7 keV and the bandpass was 0.2 to 12 keV. Compared to Athena/X-IFU, LEM will have $\sim \times 7$ the number of imaging elements with less than twice the number of TES's and is optimized for a narrower bandpass. The LMS detector benefits significantly from the technical maturity of the Athena/X-IFU microcalorimeter. The LMS shares common design elements and mechanical/electrical interfaces with the X-IFU microcalorimeter. Much of the TRL-5/6 development work completed for the X-IFU, including studies on radiation hardness,¹⁴ lifetime,¹⁵ susceptibility to vibrations, cosmic-ray mitigation,^{16,17} thermal crosstalk,¹⁸ resolution and uniformity,^{19,20} and energy scale calibration,^{21,22} are directly relevant to LMS and have been incorporated in the design without needing new technology development.

However, some differences from Athena/X-IFU naturally exist. In particular, the TES pixel properties needed to be re-optimized to meet the LEM resolution and energy range requirements in both the single pixels and hydras. Hybrid arrays that incorporate single pixels and hydras have been developed in various forms for other proposed missions, including for Lynx,¹¹ the International X-ray Observatory²³ and although not part of the current baseline, were also considered in early versions of Athena/X-IFU.²⁴ To establish TRL-5 separately to the Athena/X-IFU detector, it was particularly important to demonstrate the implementation and performance of hydra pixels in a hybrid array configuration. In Sec. 2.3, we outline the key development work that was completed for the LMS array, focusing on the development areas that are different to those previously demonstrated for Athena/X-IFU.

2.3 Optimizing the LMS Detector Array

2.3.1 Pixel design

The LMS TES pixel design is based around the same Mo/Au bilayer technology developed for Athena/X-IFU. However, to optimize for high resolution over a narrower energy range, we implemented several adjustments. First, the absorber composition is changed from the thick Bi (5 μm)/Au(1 μm) design that Athena/X-IFU uses, to 0.54 μm Au-only design. The Bi/Au composite design was needed to provide low heat-capacity (C) with high stopping power for x-rays at energies up to 12 keV. The reduced energy range of LEM means we can achieve unity stopping power at 1 keV with a significantly thinner Au absorber and without the need for an additional Bi layer. Simultaneously, the lower heat-capacity of this design enables improved spectral resolution over LEM's narrower energy range ($\Delta E \propto \sqrt{C}$). Using single layer, Au absorbers have some significant benefits; it makes the fabrication easier and eliminates any possible ageing effects associated with the oxidization of the Bi,¹⁵ which can adversely affect the energy resolution. Au has near unity reflectivity to long wavelength radiation (compared to 40% for Bi²⁵), which makes the absorbers less sensitive to stray power loading and shot noise.

Previously, we have developed a process to fabricate mechanically robust absorbers as thin as ~ 0.2 μm thick on the same pixel pitch as LEM; thus the 0.54 μm baseline for LEM is comparatively straightforward. Figure 3 shows the total absorber quantum efficiency (QE = vertical stopping power \times fill fraction) as a function of energy. Also shown is a scanning tunneling microscope (SEM) of a LEM absorber demonstrating a thickness of 0.54 μm Au with 1.5 μm gaps between pixels. This provides 99% fill-factor and 100% vertical stopping power at an energy of 1 keV which is needed to satisfy the LEM effective area requirements.

In addition, the transition temperature, T_C , of the devices is reduced from 90 to 55 mK (the LEM cryogenic chain supports 40 mK heat-sink temperature with high cooling capacity). Lower T_C enables low total heat capacity and low thermal noise ($\Delta E \propto T^{3/2}$) while ensuring the pixels are sufficiently slow to match the bandwidth and dynamic range of the TDM readout. The single

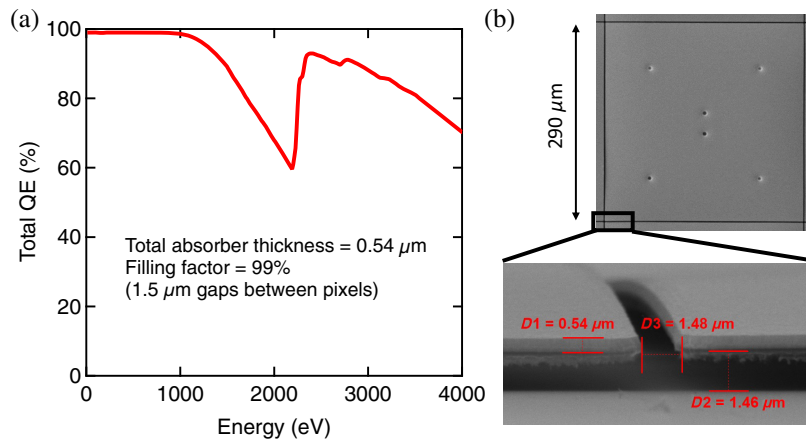


Fig. 3 (a) Total QE of the LMS pixels as a function of energy. This is defined as the vertical stopping power multiplied by the array filling fraction. (b) SEM image of a LEM absorber with the appropriate pitch ($290\ \mu\text{m}$), thickness ($0.54\ \mu\text{m}$), and gaps between pixels ($1.5\ \mu\text{m}$) needed for LEM.

pixels and hydras are implemented with the same TES geometry and absorber thickness. Because the hydras have 4 pixels for 1 TES, they have $\times 4$ the heat capacity of the single pixels and $\times 2$ worse energy resolution. The Athena/X-IFU TES consists of a Mo/Au proximity effect bilayer of size $50\ \mu\text{m} \times 50\ \mu\text{m}$ with Nb biasing leads and Au “banks” that run along the edges of the TES to ensure uniform edges.^{26,27} For LEM, we have reduced the width of TES to $15\ \mu\text{m}$ and adjusted the bilayer thickness, in combination this has enabled us to achieve the desired transition temperatures in the range 55 to 60 mK. Figure 4 shows a schematic diagram of a LEM hydra showing the anatomy of the TES pixel. The TES sits atop of a $0.5\ \mu\text{m}$ thick SiN membrane that provides the weak thermal link to the heat-bath. The absorbers are supported above the TES and membrane using 6 Au pillars. The single pixel devices have a square $200\ \mu\text{m}$ membrane, whereas the hydra has a single four-leaf clover shaped membrane of spatial extent of $450\ \mu\text{m}$. In the hydra design, 1 absorber is directly coupled to the TES via 1 of its support columns, whereas the other 3 are decoupled using Au links ($200\ \text{nm}$ thick and $2\ \mu\text{m}$ wide) of varied lengths, tuned to provide the desired hydra pulse shapes. We have successfully demonstrated hydras with up to 25 absorbers for mission concepts such as NASA’s Lynx.⁶ Because of the large number of absorbers, the Lynx hydra design necessitated a complex thermal network, where the pixels are arranged in

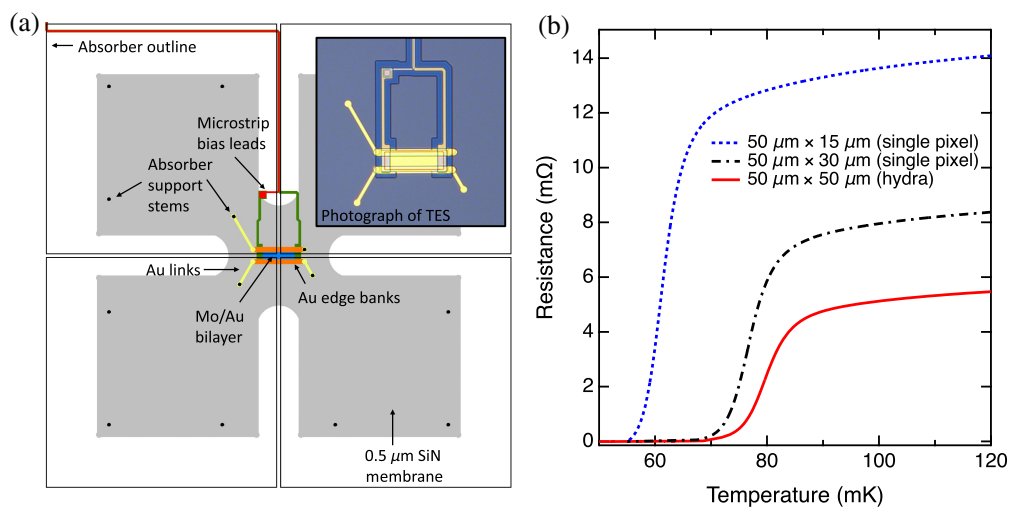


Fig. 4 (a) Schematic layout of a hydra showing the key components of the pixel design. The inset shows an optical micrograph of the TES before the membrane has been back etched and the absorbers deposited. (b) Measured resistance versus temperature curves for three TES pixels with widths of 50 (Athena/X-IFU design), 30, and $15\ \mu\text{m}$. We have baselined the $50\ \mu\text{m} \times 15\ \mu\text{m}$ TES for both the LEM single pixels and hydras.

hierarchical “tree” geometry. The 4-pixel design we are pursuing for LEM, however, is arranged in a “star” geometry where all pixels connect directly to the TES. This design is straightforward to implement, making the layout, modeling, and analysis, comparatively simple.

Figure 4 also shows the measured resistance versus temperature curves for three TESs of different widths (derived from current–voltage measurements), but all fabricated with the same Mo/Au bilayer deposition. The reduction in transition temperature with width is attributed to the lateral proximity effect from the metal banks along the edge of the TES. The normal conducting Au banks proximitize laterally into the superconducting Mo/Au TES, suppressing the effective transition temperature of the device.²⁸ As the Mo/Au width is decreased, the T_C suppression from the banks increases. A consequence of the increased aspect ratio of the device is that its normal state resistance is also increased. The higher resistance of the baseline LEM TESs compared to the $50 \times 50 \mu\text{m}$ devices baselined for Athena/X-IFU does not directly affect the performance of the pixels, but it does change the dimensioning of the readout and bias circuit parameters, such as the shunt resistor (R_s) used to voltage bias the TES, the bandwidth limiting Nyquist inductance (L) used to optimally match the bandwidth of the pixels to that of the readout, and the mutual inductance that couples the TES circuit to the SQUID readout (M_{in}). These will be discussed further in Sec. 2.4 and in Ref. 13.

The reduction of the TES width has added benefits to the LMS design related to the magnetic field sensitivity of the pixels. A TES is sensitive to the magnetic field perpendicular to the plane of the detector. Time varying magnetic fields, δB , inside the focal plane assembly can result in changes in the detector response from event-to-event,²¹ which ultimately manifests as a drift in the measured photon energy δE . This can degrade the spectral resolution of the detector and complicate the calibration of the energy scale. In general, a device with reduced perpendicular area should be less sensitive to external magnetic fields. However, the dependency of the energy gain sensitivity, $\delta E/\delta B$, on geometry is complicated by inhomogeneity of the current flow through the TES and the self-induced magnetic field generated from the current flowing in the TES and bias leads. For our TESs of lengths in the range 50 to 75 μm , we have empirically found that $\delta E/\delta B$ scales non-linearly with the width of the device.²⁷ The gain sensitivity also scales approximately linearly with photon energy and is not strongly dependent on device parameters such as heat-capacity or transition shape. Thus, the lower energy range of the LEM pixels and the reduced pixel width are both beneficial in reducing the gain sensitivity. We have recently measured $\delta E/\delta B = 7 \text{ meV/nT}$ at 1.5 keV on LMS pixels of width 15 μm ,²⁹ almost $\times 300$ lower than the 2.0 eV/nT at 7 keV measured for Athena/X-IFU pixels of width 50 μm .²¹ The low field sensitivity of the pixels is important to the LMS focal plane assembly design, enabling a reduction in the magnetic shielding requirements, and thus smaller, lower mass magnetic shields.

2.3.2 Implementation in hybrid arrays

Hybrid arrays may include pixels of different pitch, absorber composition, and TES transition temperature (or shape) fabricated on a single substrate, and thus enable the flexibility to design different parts of the focal plane to achieve different performance requirements. The hybrid focal-plane array for LEM provides better spectral resolution and count-rate capability in the central portion of the array using single pixel TESs while the use of hydras in the outer portion of the array maximizes the FoV, without adding significant technical complexity to the focal plane array and assembly. Since the TES design, the absorber pitch and the absorber thickness are the same for both the single pixels and hydra portion of the array, the implementation of the LMS hybrid array is straightforward. The only differences are the need for different SiN membrane geometries for the hydras and single pixels, and the addition of a metal link layer to connect the hydra absorbers to the TES. The SiN is released from the substrate using a deep reactive ion etch (DRIE) from the backside of the Si wafer. We have successfully optimized our DRIE process to simultaneously back-etch the different sized membranes needed for single pixel and hydras in a large format (1k-pixel) hybrid array. Different back-etch geometries have been studied for the hydra, including a simple large square membrane and a four-leaf clover geometry. The clover leaf membrane was designed to match more closely the size of single pixel membrane and thus make it easier to fabricate, since the etch rate depends on the size of the opening. However,

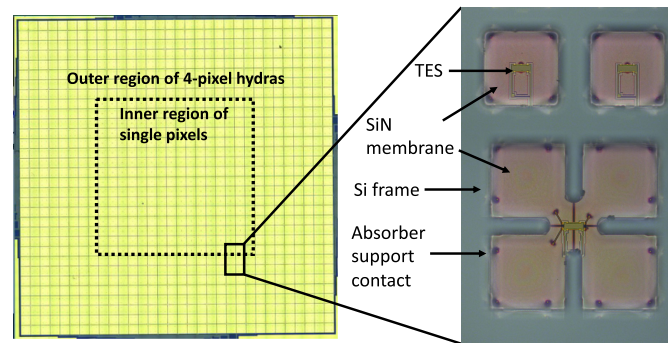


Fig. 5 Photograph of a 1k-pixel LMS hybrid array that includes both single pixel and hydra devices. Also shown is a zoom-in of the backside of the chip showing both pixel types. Visible is the Si frame, SiN membranes, and through the membranes the outline of the various TES features can be seen.

no difference was observed in the yield between the large square membrane and clover-leaf design, and in practice either geometry can be used. Figure 5 shows an optical photograph of a 1k LMS array that includes a central region of 256 pixels surrounded by 192 4-pixel hydras. Also shown is a zoom-in view of the backside of the chip showing both the pixel types. The features of the TES are visible through the membrane, showing the outline of the TES, hydra links, and the absorber support contacts. This image shows the clover-leaf membrane design for the hydra.

The measured energy histograms for representative pixels in a prototype LMS array of 1k pixels are shown in Fig. 6. We achieved a full-width-at-half-maximum spectral resolution of $\Delta E_{\text{FWHM}} = 0.90 \pm 0.02$ eV in a single pixel and 1.92 ± 0.02 eV for a 4-pixel hydra (4 pixels summed) measured using Al-K α x-rays (1.5 keV). Furthermore, the position discrimination was successfully demonstrated in the hydras down to energies of ~ 200 eV. The detailed characterization of these first pixels (including noise properties, pulse shape, transition shape, etc.) are reported in Ref. 29. These results demonstrate that the LMS pixel designs can achieve the desired performance requirements in a large format hybrid array and were key to establishing TRL-5 for the LMS detector.

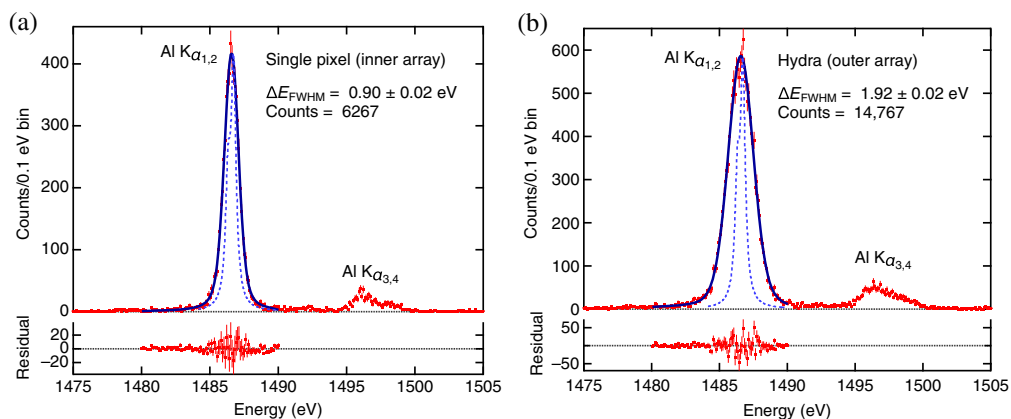


Fig. 6 Energy histograms for (a) a single pixel and (b) a four-pixel hydra (all 4 pixels summed) measured in a prototype LEM 1k pixel array. Data are measured using a fluorescent Al-K α x-ray source which emits photons of energy 1.5 keV. The dashed lines are the assumed natural line shapes for the Al-K α complex from literature^{30–32} and the solid lines are the fits to the data points. To avoid potential bias in the fitted energy resolution from the K α satellite lines whose positions are not well established, we fit to a limited energy range around the K $\alpha_{1,2}$ emission peaks only. The fitted energy resolutions are $\Delta E_{\text{FWHM}} = 0.90$ eV and $\Delta E_{\text{FWHM}} = 1.92$ eV for the single pixel and hydra respectively. Further details on the pixel performance can be found in Ref. 29.

2.4 LMS Parameters and Performance Characteristics

2.4.1 Detector and readout parameters

The baseline properties of the LMS pixels are listed in Table 2 and are derived from the characterization presented in Ref. 29. Since the TES design is the same for both pixel types, the TES transition shape (parameterized by the transition parameters $\alpha = T/R \partial R/\partial T$, $\beta = I/R \partial R/\partial I$) and noise properties are also very similar. The hydras naturally have $\times 4$ the total heat-capacity and have larger thermal conductance (G_b) to the heat-bath. For a TES on a thin SiN membrane, G_b scales by the phonon emitting perimeter of the device. Thus, the absorber support pillars that contact the membrane, and the metallic thermal links both contribute to a factor of almost $\times 2$ higher G_b in the hydra pixels. Typically, a large inductance (L) is used in series with the TES to slow the rise of the pulse and reduce the dynamic range requirement for the readout, enabling the lowest possible readout noise.⁴ The important dimensioning parameter is the “slew-rate” of the pixel, which is the maximum change in current in the TES circuit $di/dt|_{\max}$, at the maximum energy range of interest (which is 2 keV for LEM). For the hydra, this is set by the pixel directly coupled to the TES with the fastest rise-time. Based on our characterization of the single pixels and the hydras, we find that the peak slew-rates are roughly the same for a given circuit inductance L and x-ray energy. This is convenient because it means that the same TDM chips can be used to readout both pixel types. We budget 65 mA/s at 2 keV for the LMS with a baseline shunt resistance value of $R_s = 100 \mu\Omega$ and a circuit inductance of $L = 1.51 \mu\text{H}$. To accommodate the peak slew-rate within the dynamic range requirements of the TDM readout (while multiplexing 60 rows in a TDM column), we choose a mutual input coupling of the TES to the first stage SQUID input of $M_{\text{in}} = 820 \text{ pH}$. These components are situated on the TDM readout chips and

Table 2 Pixel, bias-circuit, read-out parameters and performance metrics for the LMS pixels.

Parameter	Single pixel	Hydra
T_C (mK)–transition temperature	57	57
T_b (mK)–bath temperature	40	40
R_0 (m Ω)–bias point resistance	1.5	1.6
G_b (pW/K)–bath conductance	22	42
C (pJ/K)–heat capacity	0.22	0.86
α ($= T/R \text{ dR/dT}$)–transition parameter	476	577
β ($= I/R \text{ dR/dI}$)–transition parameter	37	32
I_0 (μA)–TES current	13	17
P_0 (pW)–power dissipation	0.26	0.47
L_{crit} –critical damping inductance (μH)	3.9	4.0
L (μH)–chosen circuit inductance	1.51	1.51
R_S ($\mu\Omega$)–shunt resistor	100	100
M_{in} (pH)–SQUID mutual input inductance	820	820
$di/dt _{\max}$ (mA/s)–peak slew-rate at 2 keV	65	65
τ_+ (ms)–decay time constant	2.1	4.1
f_{eff} (Hz)–information bandwidth of pixel	265	150
t_{rec} –high resolution record length	8192 samples/79 ms	8192 samples/79 ms
i_n (pA/ $\sqrt{\text{Hz}}$)–white readout noise floor	12	12
ΔE_{FWHM} (eV)–pixel resolution	0.92	1.94

are easily accommodated in pre-existing Athena/X-IFU designs, requiring only minor adjustments. Details of the readout noise contribution to the total system performance will be discussed in Sec. 2.4.2. Further information of the TDM development for Athena/X-IFU and LEM can be found elsewhere.^{4,13}

2.4.2 Energy resolution budget

Table 3 shows the currently assumed ERB for the LMS detector. The detector performance requirements for the LMS are 1.3 and 2.5 eV FWHM at 1 keV for the single pixels and hydras, respectively. The energy resolution of the LMS is dominated by the intrinsic energy resolution of the pixels themselves; however, many system parameters contribute to the overall performance of

Table 3 LMS ERB at 1 keV.

Parameter	Single pixel value (eV)	Hydra value (eV)
Detector array (total)	0.95	2.02
TES noise	0.91	1.95
Shunt resistor noise	0.05	0.10
Cosmic rays	0.15	0.15
Set-point variation	0.20	0.50
Readout noise (total)	0.46	0.68
Broad band white noise	0.40	0.60
Narrow band noise	0.10	0.15
1/f noise	0.15	0.20
Conducted susceptibilities	0.15	0.20
Aperture cylinder (total)	0.16	0.49
Shot noise	0.13	0.4
Puncture damage	0.06	0.2
Optical loading	0.06	0.2
Gain drifts (total)	0.41	0.45
TES B-field	0.12	0.12
TES bias	0.05	0.05
TES bath temperature	0.30	0.30
TES GHZ electric-fields	0.05	0.20
Readout	0.14	0.14
Sensitivity to other temperature stages	0.10	0.10
Micro vibrations	0.20	0.20
Crosstalk	0.15	0.15
MXS centroiding	0.30	0.30
Other contributors	0.18	0.20
CBE	1.20	2.27
Unspecified margin	0.49	1.06
Total	1.30	2.50

the instrument. The ERB contains both in-band noise terms (such as noise from the detector and readout) as well as contributions due to drifts in the system gain that cannot be readily corrected, and thus contribute noise. The root-sum-squared (RSS) of all the uncorrelated contributions provides the current best estimate (CBE) of the total system performance. We hold margin for each subsystem contribution in as well as holding additional unallocated margin at the system level. This ensures that the overall performance requirements are met. The CBE is 1.2 eV for the single pixels and 2.27 eV for the hydras, leaving 0.5 and 1 eV of unspecified margin, respectively. The budget is based on direct measurement when possible, and modeling/analysis based on the baseline LEM architecture and experience from developing the Athena/X-IFU resolution budget. The budget and margins will continue to evolve as the actual performance of each subsystem is measured. The detailed apportionment in the noise budget between the LMS subsystems is complex, and here we briefly outline the key components.

Detector array. The detector array is the largest contributor for both the single pixels and hydras (0.95/2.02 eV). This contribution is almost entirely dominated by the intrinsic noise of the TES, including the TES phonon noise, Johnson noise, and any additional excess detector noise. These values are supported by the recent measurements on representative LEM pixels.²⁹ Also included are small contributions from the Johnson noise of the shunt resistor used to voltage bias the TES, thermal noise generated by cosmic ray background events that deposit energy in the detector array and a term that accounts for performance variations due to intrinsic pixel non-uniformities, the spread of bias points in a common biased column, and the effects of non-uniformity from the environment.

Readout noise. The second largest contributor (0.46/0.68 eV) is from the warm and cold readout electronics (including noise from the front-end TDM SQUIDs, second stage amplifier SQUIDs, digital to analog converters (DACs), analog to digital converters (ADCs), and the room temperature low noise amplifier). Due to the inherent mismatch between the large open loop bandwidth needed to rapidly switch between TDM rows and the individual pixel bandwidth, broadband noise sources will be aliased into the signal band. The total broadband white noise level scales with the square-root of the number of rows in a TDM column. This is typically the dominant source of noise from the readout chain. We have conservatively chosen a total non-multiplexed white noise level of $0.35 \mu\Phi_0\sqrt{\text{Hz}}$, referred to flux in the first stage SQUID (this is slightly higher than the $0.32 \mu\Phi_0\sqrt{\text{Hz}}$ used for Athena/X-IFU to accommodate additional margin). For LEM, we have 60 rows in a TDM column, which gives a multiplexed aliasing factor of ~ 14 . With the preferred choice of $M_{\text{in}} = 820 \text{ pH}$, the budgeted TES referred white noise after multiplexing is then $12 \text{ pA}/\sqrt{\text{Hz}}$.^{4,13} To accurately assess the contribution of the noise on the pixel energy resolution, we have added randomly generated white noise to measured datasets in the limit of low readout noise. Figure 7 shows the RSS resolution broadening as a function of the white noise level. At the budgeted noise allocation of $12 \text{ pA}/\sqrt{\text{Hz}}$, the RSS contributions to the total resolution are ~ 0.40 and ~ 0.60 eV for the single pixel and hydra, respectively, which we adopt in our ERB. Other small contributing terms include $1/f$ noise, narrow band noise from the SQUID and TES biases (not subject to the aliasing factor), and conducted susceptibility from electromagnetic interference (EMI) that couples to the readout chain.

Aperture cylinder. The LMS pixels will be subject to shot noise from the thermal loading generated by the thermal filters in the aperture cylinder, and optically bright sources in the FoV. An energy resolution term is also reserved for puncture damage/pin hole defects. Shot noise is due to the Poisson fluctuation of the number of photons impacting the detector in a given amount of time. The noise contribution depends upon the spectrum of the photons as well as the properties of the pixels. The total allocation for the single pixel/hydras is 0.16/0.49 eV. Since shot noise scales with the square-root of the number of photons hitting the pixels, the $\times 4$ larger area of the hydra absorbers results in $\times 2$ higher shot noise. The remaining difference is due to the differences in the single pixel and hydra time constants.

Gain drifts. Temporal changes in detector environmental parameters, such as the heat-sink temperature at which the detectors are operated, the TESs local magnetic field environment, the

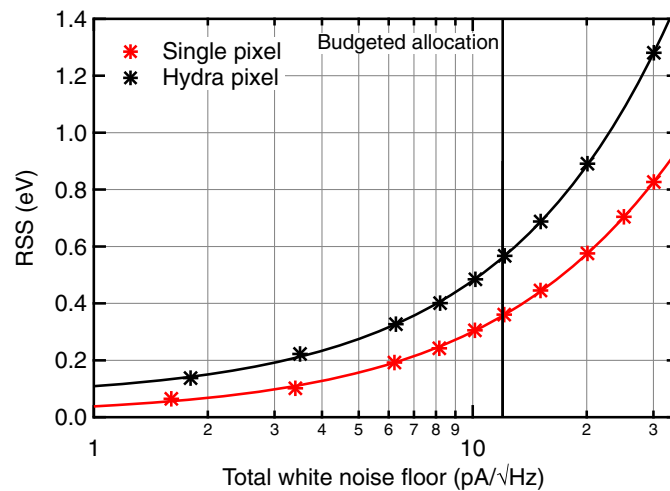


Fig. 7 RSS energy resolution degradation as a function of broad-band white readout noise for LMS single pixel and hydra detectors. The vertical line indicates the total budgeted white noise level of 12 pA/√Hz referred to the TES input.

TES bias DAC, radiative power loading, and the temperature of the readout amplifiers, may result in the drift of the energy scale function over time. Over timescales shorter than can be tracked using the on-board calibration source, these drifts cannot be corrected and thus can degrade the energy resolution. The detector magnetic field, bath temperature, and TES bias gain sensitivities have been recently measured for both LEM single pixels and hydras²⁹ and are used to consolidate the budget contributions. Unlike the noise terms, the gain sensitivities do not scale with the resolving power of the detector, thus most of these contributions are the same for both pixel types. Furthermore, the gain-related terms scale approximately linearly with energy, whereas noise sources have a much weaker energy dependence.

Crosstalk. Various sources of crosstalk exist in the detector and readout chain. This includes thermal crosstalk within the array, electrical crosstalk in the bias and readout circuit, and crosstalk due to settling transients in the high-speed signals when switching between TDM rows. The impact of crosstalk depends on the details of the source being observed. The resolution broadening scales as $E\sqrt{(r)}$, where E is the energy r is the rate. Thus, crosstalk will only become a relevant noise contributor for brighter source observations. The deterministic nature of crosstalk means that the most damaging crosstalk events which may result in broadening above the permitted allocation can be readily flagged and rejected for a small penalty in throughput (as is also planned of Athena/X-IFU). We are currently holding a 0.15 eV allocation for crosstalk for both pixel types.

Modulated x-ray source centroiding. A modulated x-ray source (MXS) will be used in flight to provide x-ray events of known energy (Al-K α x-rays at 1.5 keV). These calibration photons provide information on the detector gain drifts over time, which can be used to correct the photon energies in post-processing. Over the gain tracking period of ~ 4000 s, enough statistics will be gathered to evaluate the position of the centroid and assess the drift. Uncertainty on the centroid position broadens the energy resolution and must be accounted for in the budget. The centroid uncertainty depends on the fiducial line shape and the number of statistics gathered [scaling as $1/\sqrt{(\text{number of counts})}$]. The 0.3 eV centroid uncertainty maps to ~ 450 Al-K α events during each calibration period.

Other contributors. Small additional noise allocations not explicitly listed include crosstalk between the anticoincidence detector and the main array, the effect of cosmic-ray events on the focal-plane assembly (FPA), and microphonics.

Table 4 Event grading scheme for the LMS microcalorimeter. $\delta t_p = 55$ ms for hydra pixels and 35 ms for single pixels.

Event grade	t_{rec}	$t_{\text{pre-trig}}$	Single pixel ΔE (eV)	Hydra ΔE (eV)
High-res	79 ms (8192 samples)	5 ms (512 samples)	1.3	2.5
Mid-res	20 ms (2048 samples)	1.2 ms (128 samples)	~ 1.5	~ 2.9
Low-res	$\sim 240 \mu\text{s}$ (24 samples)	$\sim 8 \mu\text{s}$ (8 samples)	~ 15	~ 30

2.4.3 Count-rate accommodation

Photon arrival times are Poisson distributed and the count-rate accommodation of the detectors can be determined from a statistical analysis. The total time interval in which a single event can be accepted is $\delta t = \delta t_p + \delta t_n$, where δt_p is the time needed for the previous event to have decayed to a negligible level and, δt_n , the time required to process the event before the arrival of the next. The latter is defined as $\delta t_n = t_{\text{rec}} - t_{\text{pre-trig}}$, where t_{rec} is the record length used by the digital optimal filter to determine the pulse height and $t_{\text{pre-trig}}$ is the time before the trigger point (accounting for the fact that the trigger point is not at the very start of the record). The fraction of the events that can be accepted for a given rate, r , is then $f = e^{-r\delta t}$. Based on the pixel properties listed in Table 2, we choose $\delta t_p = 55$ ms for the hydras and $\delta t_p = 35$ ms for the single pixels (since they are faster pixels). However, we adopt identical record lengths of $t_{\text{rec}} = 79$ ms (8192 samples) for both. These define the high-resolution event grades. In digital optimal filtering, the choice of record length affects the achievable energy resolution.³³ The shorter the record length, the more degraded the resolution. In the ERB, this is already included as a 1.5% and 2% degradation factor for the single pixels and hydras, respectively (affecting the pixel and readout related noise terms). To maximize the instrument throughput, we can define additional event grades that have shorter record lengths, and thus slightly degraded resolution. Following similar definitions that were used for the Astro-H/SXS event grading scheme,³⁴ we define mid-resolution events with a record length of $1/4$ the high-resolution. We also define a low-resolution event grade that finds the raw pulse peak and only requires a few samples to measure. The event grades are defined in Table 4. Note that these definitions are preliminary and will be further updated as the instrument and observational needs are refined (additional intermediate event grades may also be considered). Events that do not satisfy the three primary event grades are defined as high/mid/low resolution secondary events (pile-up events landing on the tail of the previous pulse) and are not easily used for spectroscopy. The measured energy of the secondary events depends on the energy of the previous pulse and the time separation between them. As part of our future studies, we will explore methods to correct such events in post-processing, which may enable their use for spectroscopy and increase throughput at higher rates. Figure 8 shows the event grading branching ratios as a function of count-rate. The inner array of single pixels offers around $\times 6$ higher count-rate accommodation (per $15''$ pixel) compared to the hydras. This is in-part because of the larger δt_p exclusion window needed for the hydras (because the hydras pulse time constant is larger). However, the main reason is because the hydra has 4 pixels for a single TES. Consequently, they can accommodate $\times 4$ fewer events per $15''$ pixel compared to the single pixel TESs.

2.5 LMS Calibration

The LEM calibration plan (covering throughput, imaging, spectroscopy, and timing) benefits considerably from the extensive ground and inflight calibration plans developed for other microcalorimeter missions: Astro-H, the x-ray imaging and spectroscopy mission (XRISM) and Athena.^{35–39} Calibration of the LMS will use similar calibration sources that have been used for XRISM. Fluorescent target sources will be used for energy scale and line spread function calibration. The sources will be independently calibrated as transfer standards using an electron beam ion trap.⁴⁰ In addition, channel-cut crystal monochromators⁴¹ will be used to measure both the core and extended line spread function. Like XRISM and Athena, LEM will use a MXS to track on-orbit time dependent drifts in the detector gain. On LEM, the MXS will provide Al-K α x-rays at 1.5 keV. In contrast, the larger energy range of Athena requires an MXS with both

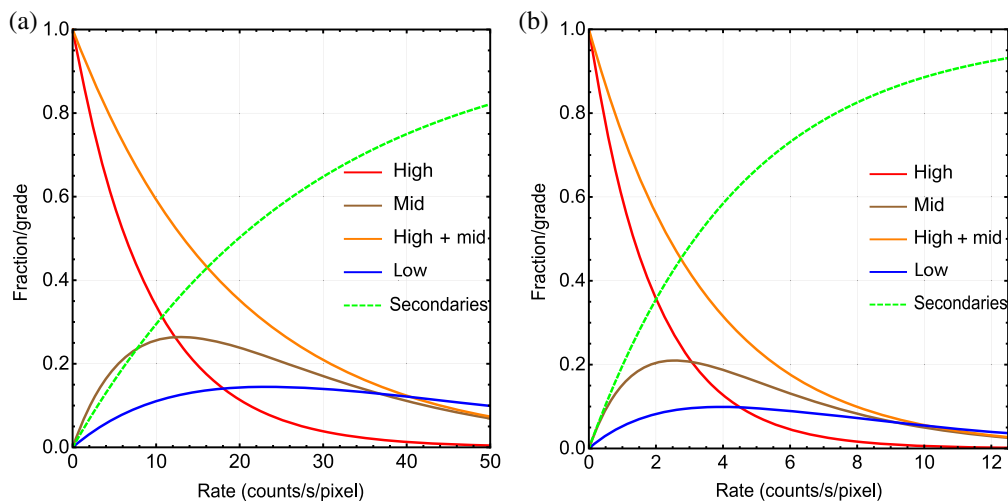


Fig. 8 Event grade branching ratios as a function of count-rate per 15 arcsec pixel for (a) single pixels and (b) hydras. High- and mid-resolution events dominate at lower count-rates before secondary events quickly dominate as the rate increases. Here, we show the total of all high/mid/low resolution secondaries combined.

Cu- $K\alpha$ at 8 keV, and Cr- $K\alpha$ at 5.4 keV.³⁹ The uncertainty on the energy scale knowledge is dominated by the MXS centroid accuracy. The intrinsically narrow Al- $K\alpha$ line width combined with the fact the energy scale requirements are defined at 0.5 keV (lower than the 1.5 keV fiducial energy used to track the gain) means that $\sim \times 10$ fewer counts are needed to satisfy the energy scale requirement compared to Athena. The centroiding accuracy also affects the energy resolution and is included as a 0.3 eV allocation in the ERB (Table 3).

2.6 Progress Toward Full Scale LMS Arrays and the Plan for Continued Maturation

Having completed our TRL-5 development plans, we are now focusing efforts on implementing high-fidelity (full-scale) LMS arrays of the appropriate form, fit, and function needed for LEM. This will be in parallel with demonstrating the LMS performance with newly fabricated TDM chips, optimized specifically for LEM. Our development plan aims to achieve TRL-6 by the end of Phase-A studies (late 2026), which will then feed into the engineering model (EM) design early in Phase-B (early 2027).

Several full-scale arrays have been fabricated for Athena/X-IFU and have been used to demonstrate various aspects of performance. This included a demonstration of the pixel performance and uniformity in a full-scale array,¹⁹ validating the heat-sinking scheme needed to mitigate the heating effects of cosmic-ray background events interacting with the Si wafer,¹⁶ and demonstrating the survivability of the array to launch loads. High-fidelity designs with the appropriate packaging needed for a flight-like system have also been demonstrated. Like the Athena/X-IFU, the preliminary LMS design can be accommodated on a single 4 inch wafer and shares the same packaging approach. Our prototype array designs are being evolved to have appropriate flight-like interfaces for mechanical mounting to the FPA, and the electrical connection to the TDM readout chips that are mounted on the side-panels of the FPA. Figure 9(a) shows a photograph of a fully fabricated prototype LMS array. The pixel array is situated in the hexagonal region in the center for the detector. The TES bias wires fan out to bond pads around the array perimeter. There are eight rows of bond pads on each of the six sides of the array. The electrical connections between the detector and TDM chips situated on the FPA side-panels are made via Al wire bonds to an around-the-corner flex that affixes to the top surface of the detector.⁴² The LMS detector will be epoxied to flexure mounts that sit underneath the array. The array is then thermally heat-sunk to the mount using Au wire bonds from the mount to metallization layers deposited on the backside of the detector chip. Figure 9(b) shows a close-up photograph of the 14k pixel array in the center of the detector chip. The pixels are on a 290 μm pitch and the array includes both individual TES pixels in the central region of the array and 4-pixel hydras in the remaining

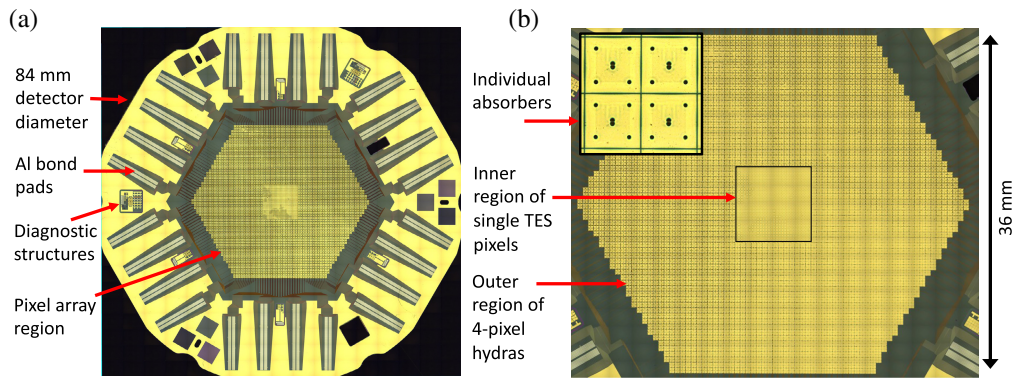


Fig. 9 (a) Tiled photograph of a fully fabricated prototype LEM array. The hexagonal TES array is in the central region of the detector chip. Eight rows of wire bond pads are positioned on each of the six sides of the array. These will be used to electrically connect the TESs to the bias and SQUID readout circuits. (b) Close-up photograph of the central region of the detector. The array includes all 14k pixels needed for LEM. The inset shows a zoom-in of 4 individual pixels ($290\ \mu\text{m}$ pitch). The six dark circles are the outline of the absorber support columns.

portion of the array. The inset shows a zoom-in view of four individual absorbers from the inner region of the array. The six dark circles visible on each absorber are the imprint of the absorber support columns that support the absorber above the substrate beneath. These first full-scale arrays will be tested through the remainder of this year, and designs will be evolved as necessary as part of our TRL-6 maturation plans through Phase-A (if LEM is selected for further study). Cosmic ray background tests previously conducted on the Athena/X-IFU microcalorimeter will be repeated (early in 2024) on a high-fidelity LMS array to validate the array's thermal design. Vibration testing and thermal cycling of the detector, mounted to flight-like sub-assemblies, are planned for later in 2024. The arrays will undergo pre- and post-vibe testing to confirm that the yield and detector performance remains unchanged. Finally, an integrated system-level demonstration will be carried out in 2025 to verify the full detection chain using the differential readout architecture needed for LEM.

3 LMS Anticoincidence Detector

Positioned 1 mm directly behind the LEM sensor array, the antico will detect $\sim 3.6\ \text{counts/s/cm}^2$ ($\sim 50\ \text{counts/s}$ over the entire LEM array) from the cosmic ray particle background environment at LEM's L1 orbit. The background is split roughly equally between the incident galactic cosmic rays and the secondary particles they generate due to interactions with the satellite and instrument structure.⁴³ The dominant cosmic-ray background is from minimum ionizing particles (MIPs) in the form of protons (75%) and alpha particles (15%), which deposit energy continuously as they traverse the main detector array and the antico beneath it. The remaining events are from electrons (with energies of 100s keV), the majority of which will also transit the detector and be seen by the antico. The resulting energy spectrum seen in the LMS pixels will be peaked at $\sim 600\ \text{eV}$.⁴⁴ Although the incident background particle flux will be the same as for Athena/X-IFU, the peak in spectrum is an order of magnitude lower energy than for Athena/X-IFU because of the thinner LMS absorbers. Singly charged MIPs (protons) will deposit $0.39\ \text{keV}/\mu\text{m}$ of Si, whereas alphas will deposit $\times 4$ this amount, thus, in the 0.5 mm Si antico we would expect a spectrum peaked at around 200 keV. Figure 10 shows a cartoon schematic of the antico concept. The energy deposited in the LMS absorbers by cosmic rays is indistinguishable from x-ray photons unless it can be rejected by coincidence or by energy (if it falls out of the 0.2 to 2 keV LEM science band). Any energy deposited in the substrate of the array is a potential noise source^{16,17} but does not contribute to the instrument background. To satisfy the background requirement of $< 2\ \text{counts/s/keV/FoV}$, the antico will have a low energy detection threshold of 20 keV and $\geq 95\%$ live time.

A TRL-9 antico has been flown on Astro-H/SXS. This antico is based around a pin diode with junction field effect transistor (J-FET) readout.⁴⁵ Although the performance of this design

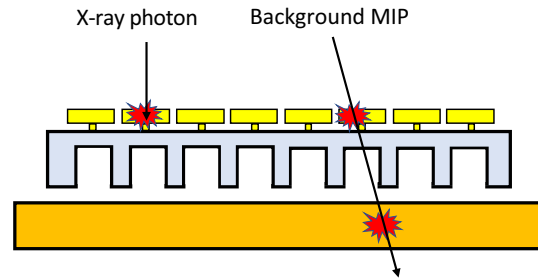


Fig. 10 Cartoon of antico concept. The antico sits directly behind the LEM main array and will identify background MIP events that could be confused with science events in the LEM bandpass.

would satisfy the LMS requirements, and it is scalable to the larger areal coverage needed for LMS, it is more convenient to use a TES based detector with SQUID readout (like the antico being developed for Athena/X-IFU^{46,47}) that can be more easily accommodated within the LMS system architecture. Our LMS antico design is based upon the large area detectors that have been developed in the dark-matter detection community.^{48,49} Such detectors have demonstrated \sim eV scale detection thresholds and 100 keV dynamic range in \sim cm² devices. These properties make such a detector ideal for an antico. We are working in close collaboration with the dark-matter detection teams at Stanford University and Northwestern University to facilitate maturation of our initial demonstration arrays. Our design utilizes a 0.5 mm thick Si crystal that absorbs the MIPs. The surface of the crystal is covered with a parallel network of quasiparticle-trap assisted electrothermal-feedback transition-edge sensors (QETs).⁴⁹ Each QET consists of a TES connected to superconducting Al films which collect athermal phonons generated by the energy deposited in the Si. These phonons break apart cooper pairs in the superconducting Al collection fins. The resulting quasi-particles diffuse along the fins and are measured as a thermal signal by the TES. In total, the antico has 12 channels, each consisting of over 100 collection cells. The antico will be read out with 3 columns of TDM each with 4 pixels. We are exploring a Mo/Au TES-based design (fabricated at NASA/GSFC)^{50,51} and a Tungsten TES-based design, W-TES (fabricated at Stanford).⁴⁹ The W-TESs are much higher resistance devices than the Mo/Au-TES and offers a different operational parameter space (transition-temperature, thermal conductance, and resistance).

The LMS antico was previously assessed at TRL-4 based on the performance of a 1 cm² single channel prototype antico that used Mo/Au TESs. This device demonstrated a detection threshold of a few hundred eV.⁵¹ To complete TRL-5, we have scaled this design to meet the \sim 14 cm² areal coverage needed for LEM and have fabricated both Mo/Au and W-TES variants.

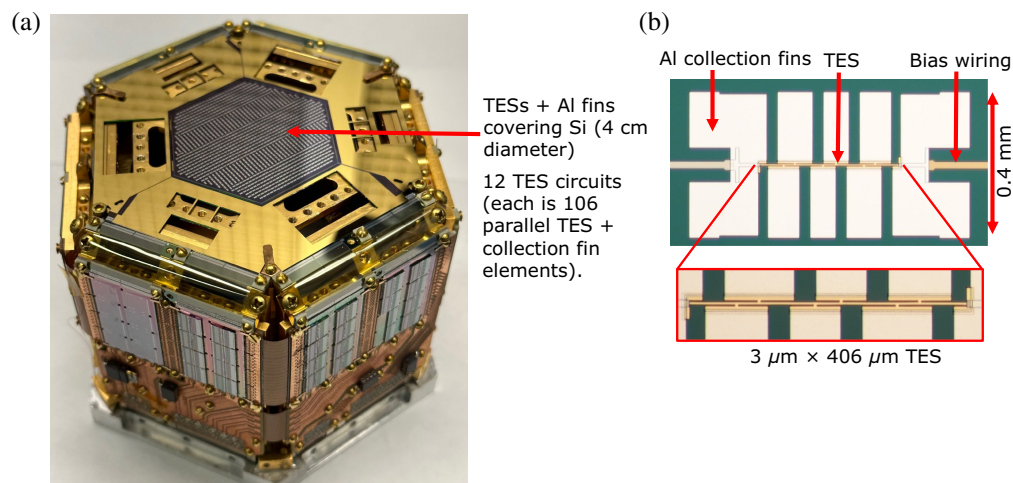


Fig. 11 (a) Prototype full-scale LMS antico detector. Consisting of 12 channels, each with a parallel network of \sim 100 collection cells on a 1 mm pitch. (b) Photograph of a single QET unit cell showing the Mo/Au TES and Al collection fins. The inset shows a zoom-in of the TES.

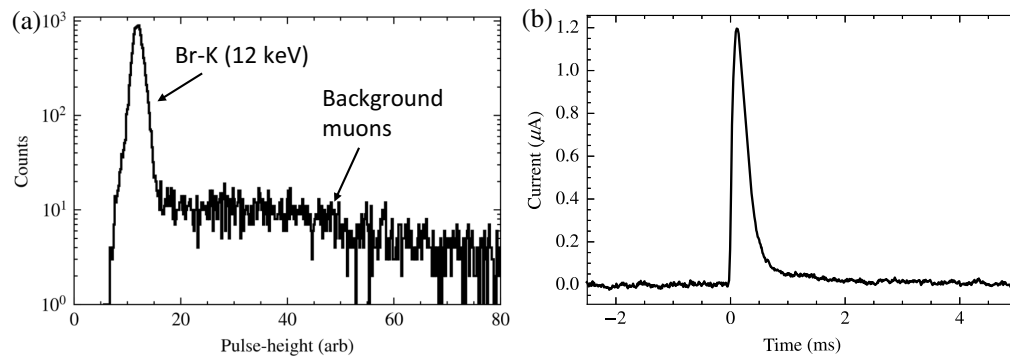


Fig. 12 (a) Measured pulse-height spectrum from one channel of a full-scale anticoncidence detector. Data are taken using 12 keV (Br-K) x-rays (incident only on that single channel). Also shown are background events from muons generated by cosmic-ray interactions in upper atmosphere. (b) Measured current pulse from a cosmic ray muon event.

Figure 11 shows a photograph of a recently fabricated full-scale prototype that is now being tested (with Mo/Au TES) as part of our TRL-5 demonstrations. Figure 12 shows a measured spectrum from collimated Br-K (12 keV) fluorescent x-rays incident on one channel of the detector. In addition to the narrow line from the Br-K events, there is a background distribution of events from muons. Muons are MIPs generated by cosmic ray interactions in the upper atmosphere (the sea level rate is ~ 1 count/min/cm²) and they deposit energy over the full area of the anticoncidence detector. A preliminary, conservative, assessment of the low energy threshold is ~ 5 keV (surpassing the 20 keV requirement). Details of the full characterization of these TRL-5 demonstration devices, including the threshold, live-time, dynamic range, and position sensitivity, will be reported at a later date.

We will continue to evaluate the performance of these demonstration arrays, selecting the best candidate design to carry forward as we evolve the concept toward a higher-fidelity flight-like design with appropriate electrical and mechanical interfaces. As with the main array development, we plan to demonstrate TRL-6 before the end of Phase-A, in time for the EM design release early in Phase-B.

4 Conclusion

We have developed a detailed design concept for the LMS microcalorimeter array and anticoincidence detector that meets the scientific needs of LEM. The LMS microcalorimeter leverages the significant investment made in developing the Athena/X-IFU microcalorimeter and its technical maturity. We have demonstrated the required detector performance (energy resolution and position sensitivity) in a k -pixel array that contains both single pixels and hydra detectors. The LMS main array is currently at TRL-5, and we are now fabricating full scale flight-like prototypes. Both main array and anticoncidence detector are on a development path that will demonstrate TRL-6 before the EM design release at the end of Phase-A (if selected for continued study).

Code, Data and Material Availability

Data supporting the findings and conclusions are presented in the paper. Raw data files can be made available upon request.

Acknowledgments

This paper is based upon work supported by NASA (Award No. 80GSFC21M0002).

References

1. R. Kraft et al., “Line Emission Mapper (LEM): probing the physics of cosmic ecosystems,” arXiv:2211.09827 (2023).
2. D. Patenaude et al., “The Line Emission Mapper: A PI-led NASA probe optimized for understanding the role of cosmic feedback on all scales,” *J. Astron. Telesc. Instrum. Syst.* (2023).

3. L. Gottardi and S. Smith, “Transition-edge sensors for cryogenic x-ray imaging spectrometers,” in *Handbook of X-ray and Gamma-ray Astrophysics*, C. Bambi and A. Santangelo, Eds., Springer, Singapore (2023).
4. H. Akamatsu et al., “Signal readout for transition-edge sensor x-ray imaging spectrometers,” in *Handbook of X-ray and Gamma-ray Astrophysics*, C. Bambi and A. Santangelo, Eds., Springer, Singapore (2023).
5. S. J. Smith et al., “Development of position-sensitive transition-edge sensor x-ray detectors,” *IEEE Trans. Appl. Supercond.* **19**(3), 451–455 (2009).
6. S. J. Smith et al., “Toward 100,000-pixel microcalorimeter arrays using multi-absorber transition-edge sensors,” *J. Low Temp. Phys.* **199**, 330–338 (2020).
7. S. J. Smith et al., “Multiabsorber transition-edge sensors for x-ray astronomy,” *J. Astron. Telesc. Instrum. Syst.* **5**, 021008 (2019).
8. T. Takahashi et al., “Hitomi (ASTRO-H) X-ray astronomy satellite,” *J. Astron. Telesc., Instrum. Syst.* **4**, 021402 (2018).
9. J. S. Adams et al., “First flight performance of the Micro-X microcalorimeter X-ray sounding rocket,” *J. Astron. Telesc. Instrum. Syst.* **9**(3), 034001 (2023).
10. D. Barret et al., “The Athena x-ray integral field unit: a consolidated design for the system requirement review of the preliminary definition phase,” *Exp. Astron.* **55**, 373–426 (2023).
11. S. R. Bandler et al., “Lynx x-ray microcalorimeter,” *J. Astron. Telesc. Instrum. Syst.* **5**(2), 021017 (2019).
12. J. A. Gaskin et al., “Lynx X-ray observatory: an overview,” *J. Astron. Telesc. Instrum. Syst.* **5**(2), 021001 (2019).
13. S. R. Bandler et al., “The Line Emission Mapper microcalorimeter spectrometer (LMS),” *J. Astron. Telesc. Instrum. Syst.* **9**(4), 041002 (2023).
14. S. Beaumont et al., “Effect of space radiation on transition-edge sensor detectors performance,” *IEEE Trans. Appl. Supercond.* **33**(5), 1–6 (2023).
15. S. Beaumont et al., “Long term performance stability of transition-edge sensor detectors,” *IEEE Trans. Appl. Supercond.* **33**(5), 1–6 (2023).
16. S. V. Hull, et al., “Characterizing thermal background events for Athena X-IFU,” *IEEE Trans. Appl. Supercond.* **33**(5), 1–6 (2023).
17. P. Peille et al., “Quantifying the effect of cosmic ray showers on the x-IFU energy resolution,” *J. Low Temp. Phys.* **199**, 240–249 (2020).
18. A. R. Miniussi et al., “Thermal crosstalk measurements and simulations for an x-ray microcalorimeter array,” *J. Low Temp. Phys.* **199**(3–4), 663–671 (2020).
19. K. Sakai et al., “Demonstration of a full-scale brassboard TES microcalorimeter array for the Athena X-IFU,” *IEEE Trans. Appl. Supercond.* **33**(5), 1–5 (2023).
20. S. J. Smith et al., “Performance of a broad-band, high-resolution, transition-edge sensor spectrometer for x-ray astrophysics,” *IEEE Trans. Appl. Supercond.* **31**(5), 1–6 (2021).
21. S. J. Smith et al., “Correcting gain drift in TES detectors for future x-ray satellite missions,” *IEEE Trans. Appl. Supercond.* **33**(5), 1–6 (2023).
22. M. C. Withoef et al., “Correcting energy estimation errors due to finite sampling of transition-edge sensor data,” *J. Low Temp. Phys.* **209**, 1000–1007 (2022).
23. R. L. Kelley et al., “The x-ray microcalorimeter spectrometer for the international X-ray observatory,” *J. Low Temp. Phys.* **1185**, 757–760 (2009).
24. S. J. Smith, “Transition-edge sensor pixel parameter design of the microcalorimeter array for the x-ray integral field unit on Athena,” *Proc. SPIE* **9905**, 99052H (2016).
25. R. Hummatov et al., “Quantum efficiency study and reflectivity enhancement of Au/Bi absorbers,” *J. Low Temp. Phys.* **199**, 393–400 (2020).
26. A. R. Miniussi et al., “Performance of an x-ray microcalorimeter with a 240 μm absorber and a 50 μm TES bilayer,” *J. Low Temp. Phys.* **193**, 337–343 (2018).
27. N. A. Wakeham et al., “Refinement of transition-edge sensor dimensions for the x-ray integral field unit on Athena,” *IEEE Trans. Appl. Supercond.* **33**(5), 1–6 (2023).
28. J. E. Sadleir et al., “Proximity effects and nonequilibrium superconductivity in transition-edge sensors,” *Phys. Rev. B* **84**(18), 184502 (2011).
29. N. A. Wakeham et al., “Characterization of the microcalorimeters developed for the Line Emission Mapper,” *J. Astron. Telesc. Instrum. Syst.* (2023).
30. M. O. Krause and J. H. Oliver, “Natural widths of atomic K and L levels, $K\alpha$ X-ray lines and several KLL Auger lines,” *J. Phys. Chem. Ref. Data* **8**, 329 (1979).
31. D. W. Fischer and W. L. Baun, “Diagram and nondiagram lines in K spectra of aluminum and oxygen from metallic and anodized aluminum,” *J. Appl. Phys.* **36**, 534 (1965).
32. B. Nordfors, “A note on the Al $K\alpha_3$ α_4 lines in metal and oxide,” *Proc. Phys. Soc. A* **68**, 654 (1955).
33. W. B. Doriese et al., “Optimal filtering, record length, and count rate in transition-edge-sensor microcalorimeters,” *AIP Conf. Proc.* **1185**, 450 (2009).

34. Y. Ishisaki et al., “In-flight performance of pulse-processing system of the ASTRO-H/Hitomi soft x-ray spectrometer,” *J. Astron. Telesc. Instrum. Syst.* **4**(1) 011217 (2018).
35. M. E. Eckart et al., “Ground calibration of the Astro-H (Hitomi) soft x-ray spectrometer,” *J. Astron. Telesc. Instrum. Syst.* **4**(2), 021406 (2018).
36. M. A. Leutenegger et al., “In-flight verification of the calibration and performance of the ASTRO-H (Hitomi) soft x-ray spectrometer,” *J. Astron. Telesc. Instrum. Syst.* **4**(2), 021407 (2018).
37. T. Omama, “Relative timing calibration of the Resolve x-ray microcalorimeter onboard XRISM using the modulated x-ray source,” *Proc. SPIE* **12181**, 1218162 (2022).
38. E. D. Miller et al., “Planning in-flight calibration for XRISM,” *Proc. SPIE* **11444**, 1144426 (2020).
39. E. Cucchetti et al., “Energy scale calibration and drift correction of the X-IFU,” *Proc. SPIE* **10699**, 106994M (2018).
40. G. V. Brown et al., “A brief overview of the fusion and astrophysics data and diagnostic calibration facility,” *Proc. SPIE* **7732**, 77324Q (2010).
41. M. A. Leutenegger et al., “Simple, compact, high-resolution monochromatic x-ray source for characterization of x-ray calorimeter arrays,” *Rev. Sci. Instrum.* **91**(8), 083110 (2020).
42. H. Geoffray et al., “Design of the detection chain for Athena X-IFU,” *Proc. SPIE* **12181**, 121810M (2022).
43. S. Lotti et al., “Review of the particle background of the Athena X-IFU instrument,” *ApJ* **909**, 111 (2021).
44. S. Lotti, “First assessment of non-X-ray background in Line Emission Mapper (LEM) focal plane detector,” technical note and personal communication with C. Kilbourne (2023).
45. C. A. Kilbourne et al., “Design, implementation, and performance of the Astro-H SXS calorimeter array and anticoincidence detector,” *J. Astron. Telesc. Instrum. Syst.* **4**(1), 011214 (2018).
46. C. Macculi et al., “The cryogenic anticoincidence detector for ATHENA X-IFU: the project status,” *J. Low Temp. Phys.* **199**, 416–424 (2020).
47. M. D’Andrea et al., “ATHENA X-IFU demonstration model: first joint operation of the main TES array and its cryogenic AntiCoincidence detector (CryoAC),” *J. Low Temp. Phys.* **209**, 433–440 (2022).
48. I. Alkhatib et al., “Light dark matter search with a high-resolution athermal phonon detector operated above ground,” *Phys. Rev. Lett.* **127**, 061801 (2021).
49. R. Ren et al., “Design and characterization of a phonon-mediated cryogenic particle detector with an eV-scale threshold and 100 keV-scale dynamic range,” *Phys. Rev. D* **104**(3), 032010 (2021).
50. C. N. Bailey et al., “Development of a TES-based anticoincidence detector for future x-ray observatories,” *J. Low Temp. Phys.* **167**(3–4), 236–241 (2012).
51. S. E. Busch et al., “Characterization of a prototype TES-based anticoincidence detector for use with future x-ray calorimeter arrays,” *J. Low Temp. Phys.* **184**(1–2), 23–29 (2016).

Stephen J. Smith is a research astrophysicist at NASA Goddard Space Flight Center. He received his MPhys degree in physics with space science and technology in 2002 and his PhD in physics in 2006, both from the University of Leicester, United Kingdom. He is an author of ~150 published papers. His primary research interests are in the development of cryogenic detectors and systems for x-ray astronomy applications.

Simon R. Bandler is a research astrophysicist at NASA’s Goddard Space Flight Center. He received his BS degree in mathematical physics from the University of Sussex, United Kingdom and his MS and PhD degrees in physics from Brown University in 1992 and 1996, respectively. He is the author of more than 200 journal papers. His current research interests include transition-edge sensor and magnetic x-ray microcalorimeters, x-ray astrophysics, and the ESA flagship mission called Athena.

Caroline A. Kilbourne is a senior scientist in the X-ray Astrophysics Laboratory of NASA’s Goddard Space Flight Center, where she has been developing low-temperature microcalorimeters for high-resolution x-ray spectroscopy since arriving as a postdoc in 1992. Her responsibilities at Goddard have ranged from advanced detector development at the sensor level to optimizing the myriad systems and their interfaces needed to progress from a promising sensor technology to a robust, space-worthy spectrometer.

Kazuhiro Sakai is an assistant research scientist at the University of Maryland Baltimore County working at NASA Goddard Space Flight Center (GSFC). He received his PhD in physics from the University of Tokyo in 2015, was a postdoctoral researcher at Institute of Space and Astronautical Science (ISAS)/Japan Aerospace Exploration Agency (JAXA) from 2015 until he became a postdoc at NASA GSFC in 2016.

Nicholas A. Wakeham is an assistant research scientist at the University of Maryland Baltimore County working at NASA Goddard Space Flight Center (GSFC). He received his PhD in low temperature condensed matter physics from the University of Bristol in 2013, was a postdoctoral researcher at Los Alamos National Laboratory from 2013 until he became a NASA Postdoctoral Fellow at GSFC in 2016. His interests are exotic electronic states, unconventional superconductivity, and superconducting detectors.

Biographies of the other authors are not available.